1-1-2020

Acoustic Modeling Of A Uas For Use In A Hostile Fire Detection System

Keegan Kurpakus

ACOUSTIC MODELING OF A UAS FOR USE IN A HOSTILE FIRE DETECTION SYSTEM

A Thesis

Presented for the

Masters of Science at the Department of Physics and Astronomy

The University of Mississippi

by

KEEGAN KURPAKUS

May 2020

ABSTRACT

Unmanned Aerial System (UAS) usage has continually increased in recent years for both recreational and military applications. One particular military application being researched is utilizing a UAS as a host platform for Hostile Fire Detection Systems (HFDS), with particular interest being focused on multi-rotor drone platforms. The type of HFDS considered in this work is based upon acoustic sensors. An acoustic based HFDS utilizes an array of microphones to measure acoustic data and then applies signal processing algorithms to determine if a transient signal is present and if present then estimates the direction from which the sound arrived.

The main issue with employing an acoustic based HFDS on a multi-rotor drone is the high level of background noise due to motors, propellers, and flow noise. In this thesis a study of the acoustic near field, particularly relevant to microphones located on the drone, was performed to understand the noise produced by the UAS. More specifically, the causes and characteristics of the sources of noise were identified. The noise characteristics were then used to model the noise sources for multiple motor assemblies based upon position of the microphone and revolutions per minute (RPM) of the motors. Lastly, signal processing techniques were implemented to identify if transient signals are present and if present estimate the direction from which the sound arrives.

DEDICATION

I would like to dedicate this work to my friends and family who have helped and inspired me along this journey.

ACKNOWLEDGEMENTS

I would like to express my gratitude to my advisors, Dr. Wayne Prather and Dr. Garth Frazier for their guidance, vast knowledge, and inspiration for doing research. I am grateful for Dr. Joel Mobley for serving on my committee and serving as my advisor for the Physics department. I am also grateful for Dr. Xaio Di for his helpful discussions and assistance with laboratory setups. I would like to also extend my gratitude to Dr. Nathan Murray and Dr. Charles Tinney for their insight and helpful discussions.

I am also thankful for all members for all members of the National Center for Physical Acoustics and the Department of Physics and Astronomy.

Lastly I want to thank my family again for all of their support and guidance.

TABLE OF CONTENTS

ABSTRACT ii

DEDICATION iii

ACKNOWLEDGEMENTS iv

LIST OF FIGURES vii

CHAPTER 1: INTRODUCTION AND LITERATURE SURVEY 1

1.1 HOSTILE FIRE DETECTION SYSTEMS 1

1.2 LITERATURE SURVEY 3

1.3 OVERVIEW 6

CHAPTER 2: MEASUREMENTS AND EXPIREMENTAL METHOD 7

2.1 EXPERIMENTAL SETUP 7

2.2 MEASUREMENTS METHOD 10

2.3 DATA ANALYSIS METHOD 13

CHAPTER 3: RESULTS OF POWER SPECTRAL DENSITY ANALYSIS 18

3.1 LABORATORY EXPERIMENTS 18

3.2 ANECHOIC CHAMPER EXPERIMENTS 23

3.3 LOW FREQUENCY RANGE ANALYSIS 24

3.4 HIGH FREQUENCY RANGE ANALYSIS 26

3.5 MULTIPLE MOTOR CONFIGUATION 30

CHAPTER 4: ADAPTIVE FILTER FOR TRANSIENT DETECTION 34

4.1 LEAST MEAN SQUARE FILTER 34

4.2 NORMALIZED LEAST MEAN SQUARE FILTER 35

4.3 NLMS FILTER FOR TRANSIENT DETECTION 37

4.4 NLMS FILTER RESULTS 39

CHAPTER 5: CONCLUSION 44

BIBLIOGRAPHY 45

VITA 50

LIST OF TABLES

Table 4.1. Standard deviation of the error for NLMS algorithm …… 39

Table 4.2. Standard deviation of errors for smaller step sizes …… 40

Table 4.3. Standard deviation of errors with a decimation by a factor of 2 …… 41

Table 4.4. Standard deviation of errors with a decimation by a factor of 5 …… 41

Table 4.5. False alarm rate for $\alpha = 1 - 1/5e15$, D = successful detection, F = only false alarms … 42

Table 4.6. Noise level reduction …….. 42

LIST OF FIGURES

Figure 2.1. Tarot 680 Pro hexacopter …… 8

Figure 2.2. Example setup of single motor/propeller assembly …….. 8

Figure 2.3. One experimental setup in the anechoic chamber at the National Center for Physical Acoustics (NCPA), University of Mississippi …… 9

Figure 2.4. Varying microphone positions for testing in the lab …….. 11

Figure 2.5. Varying microphone positions for testing in the lab …… 11

Figure 2.6. Varying microphone positions for testing in the lab …… 12

Figure 2.7. Varying microphone positions for testing in the lab …… 12

Figure 2.8. PSD generated using the pwelch method for frequency analysis ……. 15

Figure 2.9. Background noise comparison vs noise produced by the motor/propeller assembly rotating at 4250RPM in the lab …… 16

Figure 2.10. Background noise comparison vs noise produced by the motor/propeller assembly rotating at 4250RPM in the anechoic chamber …….. 17

Figure 3.1. Microphone attached to the motor housing …… 19

Figure 3.2. Speed comparison for a microphone placed under the motor housing …… 19

Figure 3.3. Experimental setup for non-rigidly attached microphone …… 20

Figure 3.4. Comparison of microphone rigidly attached and non-rigidly attached …… 21

Figure 3.5. Microphone placed 11cm from far end of the housing and 6cm below the arm …… 22

Figure 3.6. Microphone placed 30cm from the far end of the housing and 11cm below the arm …… 22

Figure 3.7. Experimental setup in the anechoic chamber …… 23

Figure 3.8. Noise comparison between lab and anechoic chamber for identical microphone position and rotor speed …… 24

Figure 3.9. Speed comparison for single Tarot 690 quadcopter motor …… 25

Figure 3.10. Comparison of hexacopter vs quadcopter assembly at identical speeds and microphone locations …… 26

Figure 3.11. High frequency spikes …… 27

Figure 3.12. Motor spun at 4250RPM with no propeller attached …… 28

Figure 3.13. Double microphone setup in anechoic chamber …… 29

Figure 3.14. Coherence plot between microphones …… 30

Figure 3.15. Time delay between microphones …… 30

Figure 3.16. Multiple motor configuration for testing in anechoic chamber …….. 31

Figure 3.17. Multiple arm noise level comparison …… 32

Figure 4.1. Tarot 680 Pro with Zylia ZM – 1 spherical array …… 38

Chapter 1

INTRODUCTION AND LITERATURE SURVEY

1.1 Hostile Fire Detection Systems

Hostile Fire Detection Systems (HFDS) are used to detect small arms fire, rocket propelled grenades (RPG), mortars, and artillery on the battlefield. One common type of HFDS utilizes acoustic sensors to detect the acoustic waves emitted by various munitions. These acoustic waves generally come from two main sources. One source is the muzzle blast exiting the end of the weapon barrel and the other is the ballistic shock wave emitted from the projectile if it is supersonic. The acoustic wave from the muzzle blasts has most of its energy at frequencies below 500 Hz and the acoustic wave from the supersonic projectile moving through the air past the sensor array has most of its energy at frequencies above 10 kHz.

The performance of an acoustic based HFDS is strongly correlated to the signal-to-noise ratio (SNR) between the measured signal of interest and the combination of background noise sources. The ideal way to maximize performance is to improve the SNR by minimizing the background noise. In numerous cases this is not an acceptable solution due to the limiting conditions imposed for obtaining a low background environment, such as requiring the HFDS platform to remain stationary. As an example, the Raytheon Boomerang is a currently fielded HFDS system used by the US Army which works satisfactorily when stationary but which suffers

from significant performance degradation when its platform (usually a High Mobility Multipurpose Wheeled Vehicle) is in on-the-move conditions. Therefore, there is a need for the development of techniques for enabling the effective operation of HFDS's in very noisy or low SNR conditions.

There is also interest from the military for employing a HFDS on a multi-rotor drone. This allows for a mobile platform which is able to maneuver around an environment, such as a battlefield, and detect any possible hostile fire events. The main issue with employing a HFDS system on a multi-rotor drone is the high level of background noise due to motors, propellers, and flow noise. The design of most multi-rotor drones is such that each of the propellers is driven by a brushless DC electric motor inside of which there are permanent magnets on the rotor and coils of wire on the stator. The coils of wire on the stator constitute electromagnets which are controlled by an electrical signal generated by an Electronic Speed Controller (ESC). The current flowing through the stator coils create a magnetic field which interacts with the permanent magnets on the rotor resulting in a torque on the rotor causing the motor to spin. The various mechanical and electrical components of the rotating motors cause high-frequency background noise directly correlated to the revolutions per minute (RPM). Additionally, there is significant noise caused by the turbulent flow created by the spinning propellers. This high level of noise has a detrimental effect on the ability of an acoustic array mounted on the drone to detect the acoustic signals of interest.

In order to have good performance from a HFDS, the microphone array must be able to distinguish between the signal of interest and background noise. The background noise

component of the signal measured by the acoustic array will include both noise from near field sources on the drone, flow noise, as well as far-field noise due to the environment in which the system is operating. One method for combating this is in an acoustic HFDS is to run a band pass filter to focus only on the frequencies of interest which eliminates all of the noise at frequencies not within this band. An adaptive filter algorithm can also be applied to learn the background noise level of the environment and lower the false alarm rate by predicting the background noise and adjusting the filter to the current noise level.

1.2 Literature Survey

The primary subject of most acoustic rotorcraft research to date has focused on modeling the sound generated from helicopter rotors. These efforts were focused on the main rotor, but the models are considered generally valid for a range of rotor configurations. The majority of the modeling is based on by the Ffowcs Williams-Hawkings (FW-H) equation. The loading noise and thickness noise of the rotorcraft rotor is accounted for by the monopole and dipole source terms of the equation respectively. The loading noise is due to the accelerating force on the fluid by the rotating propellers, also described as the lift and drag produced on the rotor blades as they accelerate through the air. The thickness noise is caused by a sound pulse created by the rotating rotor blades displacing the air around them. [Brentner,Farassat,2003] The studies show accurate modeling of the acoustics of rotorcraft and the techniques are often used as a framework for modeling UAS that contain rotors.

A majority of previous studies on the background noise produced by UAS have focused on the far field, thus neglecting the intricate details of the noise such as the characteristics

produced by each individual motor. It has been shown that the far field acoustic signature of small multi-rotor drones can be predicted and that a majority of the noise arises from the propellers [Kloet,Watkins,Clothier,2017].The further the microphone array is from the drone the lower the noise contribution from the motors; thus most previous work has considered the motor noise as negligible. This is due to the noise level being dominated by the turbulence generated by the propellers and the blade pass frequency noise. One cause of this is that for field distances the high frequency motor noise is attenuated by the atmosphere more than the lower frequency noise of the turbulence generated by the propellers and thus its contribution is diminished.

A basic study performed in the acoustic near field showed that in addition to the main rotor harmonic noise there was also non-rotor harmonic noise. This non-rotor noise was primarily due to the motor with some additional noise being caused by the electronic speed controller. [Tinney,Sirohi,2018] It should be pointed out that this research was directed at understanding how the change in propeller dimensions and number of propellers affected the sound profile, and not the identification of noises in the near field.

Sound localization using a microphone array on a UAS has also been utilized in search and rescue applications. The open source software developed by the Honda Research Institute Japan Audition for Robotics with Kyoto University (HARK) utilizes a 16 channel microphone array on a UAS to detect whistle blasts in search and rescue attempts. It utilizes either a standard eigenvalue decomposition based MUSIC (SEVD-MUSIC) algorithm, or an incremental generalized singular value decomposition based MUSIC (iGSVD-MUSIC) algorithm. The MUSIC

algorithm is a Multiple Signal Classification used for frequency estimation. The UAS operator can choose which decomposition to use based on the situation and what information is needed. [Nakadai, *et al*,2017] The microphone array was designed such that a spherical array on poles extended out from the end of the UAS arms and the motor-propeller assemblies were treated as far-field noise allowing for more precise sound localization. Extending the microphone array arms away from the propellers decreases the noise level recorded by the microphones.

The MUSIC algorithm is also utilized in a time-frequency processing method for acoustic sensing and location. A study performed by Lin Wang and Andrea Cavallaro shows that a time-frequency processing method is able to locate a direction of arrival (DoA) of a traniseint that is captured by the acoustic array mounted on a multi-rotor drone. The proposed method also utilizes techniques for enhancing the measured signal for better DOA localization and is shown to work optimally when the array is pointed towards the sound source. [Wang,Cavallaro,2018]

Acoustic HFDS have been shown to work in shot detection and shooter localization. The accuracy of the DoA is dependent on number of microphones, their locations, and distance to the shooter. [Fernandes, Apolinário Jr., Ramos, 2017] This investigation showed that a higher number of microphones were needed to localize the DoA of a target more accurately.

A majority of previous studies have attempted to solve the problem of the drone noise through application of various data processing techniques (i.e., signal processing research). This thesis aims to explain the main components of the background noise of a multi-rotor UAS and their origins and accurately model them to aid the design of a HFDS mounted on a UAS.

1.3 Overview

Chapter 2 explains the experimental setup and methods used for UAS analysis. Chapter 3 shows the results of the UAS noise analysis. The measurements obtained were analyzed using power spectral density (PSD) plots to determine the presence and characteristics of the noise of the UAS. It is shown that various sound sources can be identified based upon the changes in the PSD due to changes in the motor speed and microphone position.

In Chapter 4, the Least Mean Square adaptive filter and the Normalized Least Mean Square adaptive filter are studied for their transient detection analysis capabilities. Chapter 5 discusses the main results and conclusions.

Chapter 2

MEASUREMENT AND EXPERIMENTAL METHOD

2.1: Experimental Setup

Measurements of the background noise environment of a multi-rotor UAS platform were first performed by employing a single arm of a Tarot 680 Hexacopter consisting of a single motor and propeller combination. An example of the Tarot 680 Hexacopter is shown in Figure 2.1 and the experimental setup in Figure 2.2. For the measurements the Tarot 680 carbon fiber tube arm was replaced with an aluminum tube of the same diameter but longer length to aid in mounting. The aluminum arm was fastened, to minimize vibrational effects, by securing it to the motor-propeller assembly similar to the standard setup for the hexacopter. Tightly mounting the arm with a three jaw chuck reduces the amount of vibrational effects when the motor is spun at high speeds, and more closely resembles the Tarot 680 build. The motor utilized was a Tarot 6S 680KV brushless electric motor that was controlled by a HobbyWing 40A electronic speed controller (ESC). The attached propeller was a Tarot 1355 carbon fiber propeller with a 13-inch diameter and 5.5-inch blade pitch.

Figure 2.1. Tarot 680 Pro Hexacopter

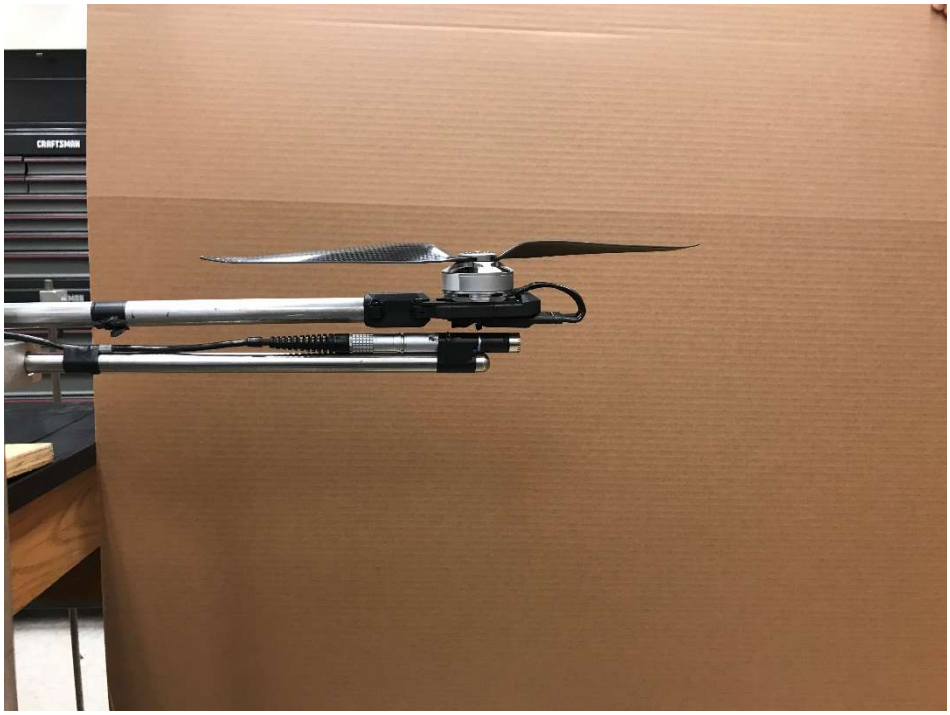

Figure 2.2. Example setup of single motor/propeller assembly.

Measurements were first conducted in a lab at the National Center for Physical Acoustics (NCPA), University of Mississippi. All measurements were conducted indoors under normal temperature and pressure conditions. After initial laboratory measurements, testing was also done in an anechoic chamber located at the NCPA with an internal measurement space volume of 36 m^3, shown in Figure 2.3.

Figure 2.3. One experimental setup in the anechoic chamber at the National Center for Physical Acoustics (NCPA), University of Mississippi

For measurements in the lab, the UAS arm was mounted 104 cm above the ground, hanging over the edge of a lab table. A 1/2" Brüel & Kjær, type-4190 microphone connected to a Brüel & Kjær Nexus Type 2691 conditioning amplifier was positioned underneath the motor-propeller housing assembly. The data collection software used was a custom program written in LabView running on a Panasonic Toughbook to record the acoustic pressure signal from the B&K microphone at a sampling rate of 50,000 samples per second (sps).

A similar method was used with a single arm motor-propeller assembly from a Tarot 690 quadcopter. The motor-propeller assembly utilized on the Tarot 690 quadcopter consists of a Tarot MT4006 320KV motor controlled by a HobbyWing 40A ESC with a 15-inch Tarot TL100D03 folding propeller. The 320KV motor has 18 coils in the center, as compared to the 24 coils in the

680KV motor used with the hexacopter. This testing was performed to determine if there was any noise phenomena unique to each motor assembly. Testing was also performed with a Lumenier 36A BLHeli_32 ESC in order to access its ability to measure the rotational speed of the motor for both the Tarot 680 and Tarot 690.

2.2: Measurements Method

Measurements were conducted by first attaching the B & K microphone directly to the bottom of the motor-propeller housing assembly and secondly mounting the microphone on a stand underneath, but not attached to the UAS arm. The motor was operated at various rotational rates ranging from 3000-6000 RPM, all measured with an optical tachometer. The stand mounted microphone was positioned at various locations along the length of the arm horizontally, as well as vertical positions below the arm. These various positions were achieved by altering the stand position and configuration both horizontally and vertically. The microphone was secured to the stand using electrical tape as seen in Figures 2.4-2.7. Due to laboratory space constraints the microphone was secured to the arm mount directly as seen in Figure 2.7 for measurements far from the propeller blade.

Figures 2.4 – 2.7. Varying microphone positions for testing in the lab.

The Nexus conditioning box was initially set for an output of 316mV/Pa amplification but adjusted as necessary for testing in various conditions to maximize measurement accuracy. Based on the location of the microphone the amplification from the Nexus box was adjusted to avoid clipping of the measured signal. The frequency range of interest for all of the measurements was from 40 Hz to 18 kHz.

2.3 Data Analysis Method

The raw data collected from the microphone was converted to a text file and analyzed using Octave Forge's signal processing package function "pwelch". This package uses Welch's method for spectral density estimation under the assumption the signal is a stationary process. A stationary process is a stochastic process whose unconditional joint probability distribution does not change when shifted in time (Gagniuc, Paul A. (2017). *Markov Chains: From Theory to Implementation and Experimentation*. USA, NJ: John Wiley & Sons. pp. 1–256). The Welch method is defined by letting the length of the segments be L, the i^{th} segment be $\{x_i[n]\}_0^{L-1}$, and the offset of successive sequences by D samples.

$$N = L + D(K-1)$$

Where N is the number of observed samples and K the number of sequences. The i^{th} sequence is defined by:

$$x_i[n] = x[n + (i-1)D]$$

$$n \in \{0,1, \dots, L-1\}$$

With the periodogram:

$$\hat{P}_M^{(i)}(f) = \frac{1}{L}\left|\sum_{n=0}^{L-1} w[n]x_i[n]e^{-j2\pi fn}\right|^2$$

The Welch spectrum estimate is given by:

$$\hat{P}_B(f) = \frac{1}{K}\sum_{i=1}^{K} \hat{P}_M^{(i)}(f)$$

[Hayes, 1996]

The results from the pwelch method in Octave Forge is presented graphically in a PSD plot that can be analyzed in the frequency domain. An example PSD of the frequency domain using the pwelch method is shown in Figure 2.8. An initial analysis of the data is presented here with further analysis and results of the PSD addressed in Chapter 3 with identification of noise sources.

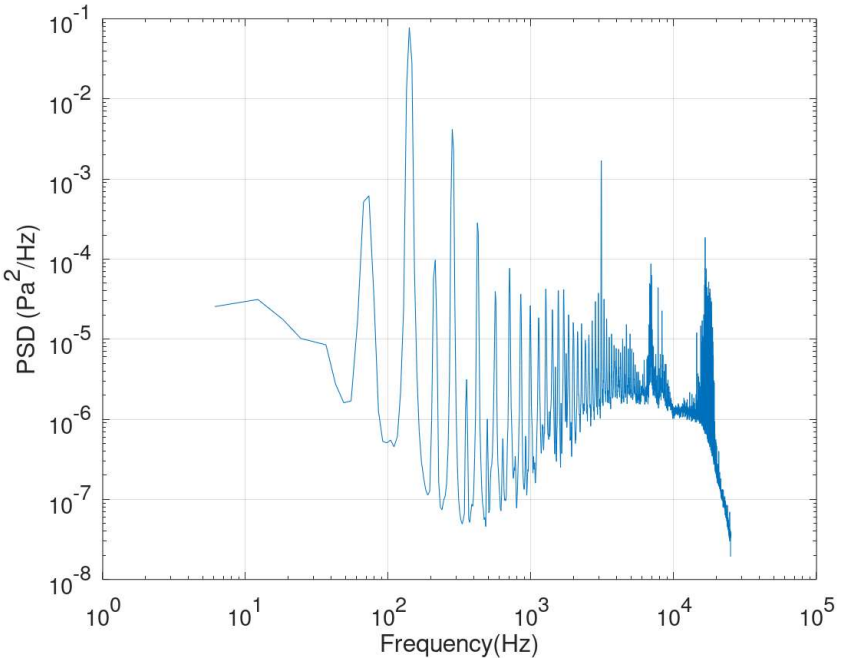

Figure 2.8. PSD generated using the pwelch method for frequency analysis

Initial analysis of the PSDs considers background noise levels of both the anechoic chamber and lab. The background noise level of the lab had a PSD between 10^{-6} and 10^{-8} Pa^2/Hz for frequencies of 10-100Hz and 10^{-8} to 10^{-12} Pa^2/Hz for frequencies of 100-12000Hz. A comparison of the room noise to a typical measurement level of motor-propeller noise relevant to this effort is shown in Figure 2.9. As can be seen the background noise of the lab is well below the noise level of the motor-propeller and therefore is not expected to be an issue in the data.

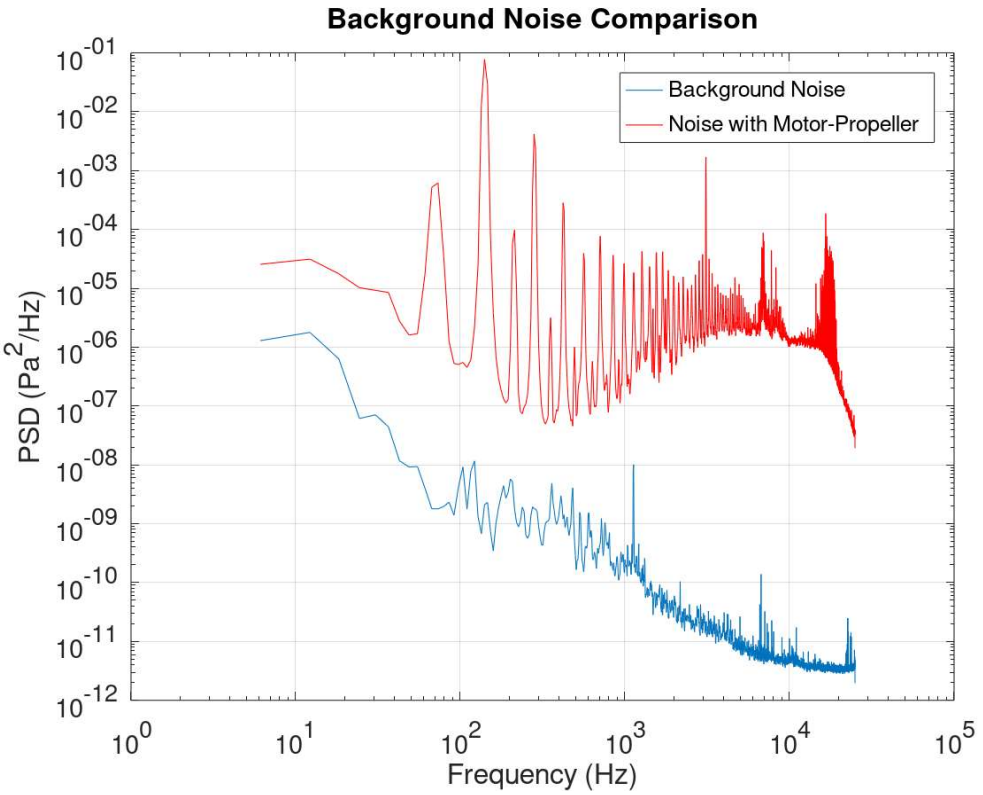

Figure 2.9. Background noise comparison vs. noise produced by the motor/propeller assembly rotating at 4250RPM in the lab

The background noise level of the anechoic chamber is lower that the lab as expected with a PSD between 10^{-11} and 10^{-12} Pa^2/Hz for frequencies above 100Hz and 10^{-6} to 10^{-11} Pa^2/Hz for frequencies between 10 and 100Hz. A comparison of the anechoic chamber noise to a typical measurement level of motor-propeller noise relevant to this effort is shown in Figure 2.10. As with the lab background noise, the anechoic chamber background noise is well below the noise of the motor-propeller and is not expected to cause an issue in the data.

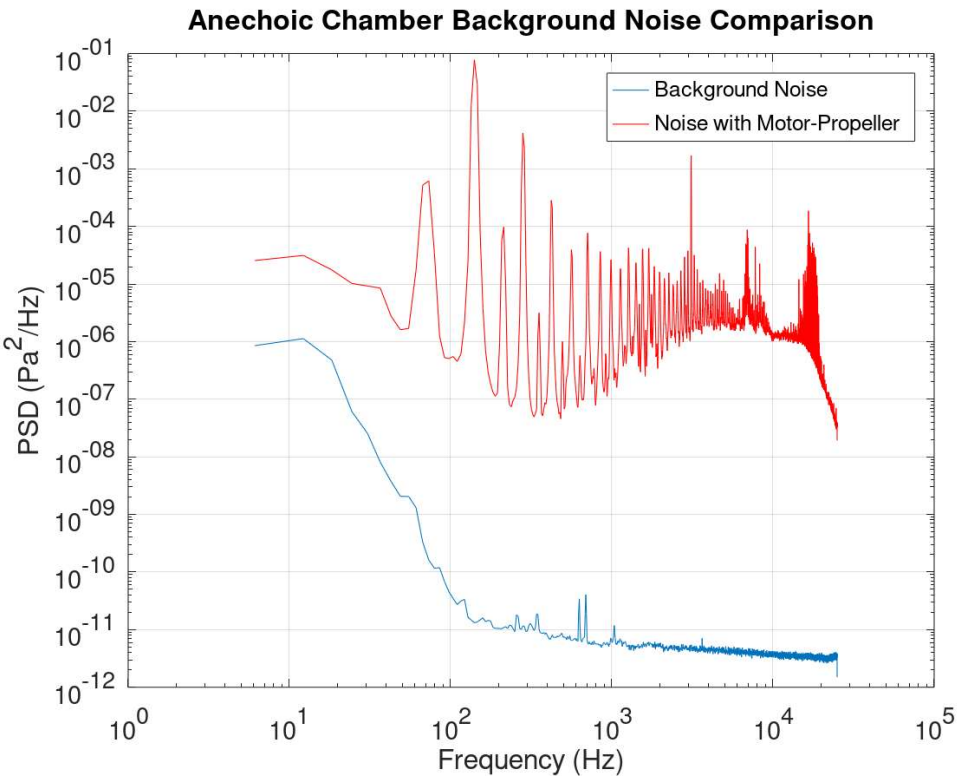

Figure 2.10. Noise comparison between the motor-propeller assembly rotating at 4250RPM in the anechoic chamber.

Chapter 3

RESULTS OF POWER SPECTRAL DENSITY ANALYSIS

3.1 Laboratory Experiments

Using the experimental setup described in Chapter 2.1, analysis was performed of the single Tarot 680 Pro hexacopter motor-propeller assembly. Initial measurements were performed with the B&K microphone attached directly below the assembly, as shown in Figure 3.1. The rotational rate of the motor was varied between 1300RPM and 6250RPM as measured with an optical tachometer. Figure 3.2 displays the changing PSD as the motor is rotated at various rates. The general trend of the response is for the entire curve to shift towards the higher frequencies as the rotational rate is increased.

Figure 3.1. Microphone attached to the motor housing

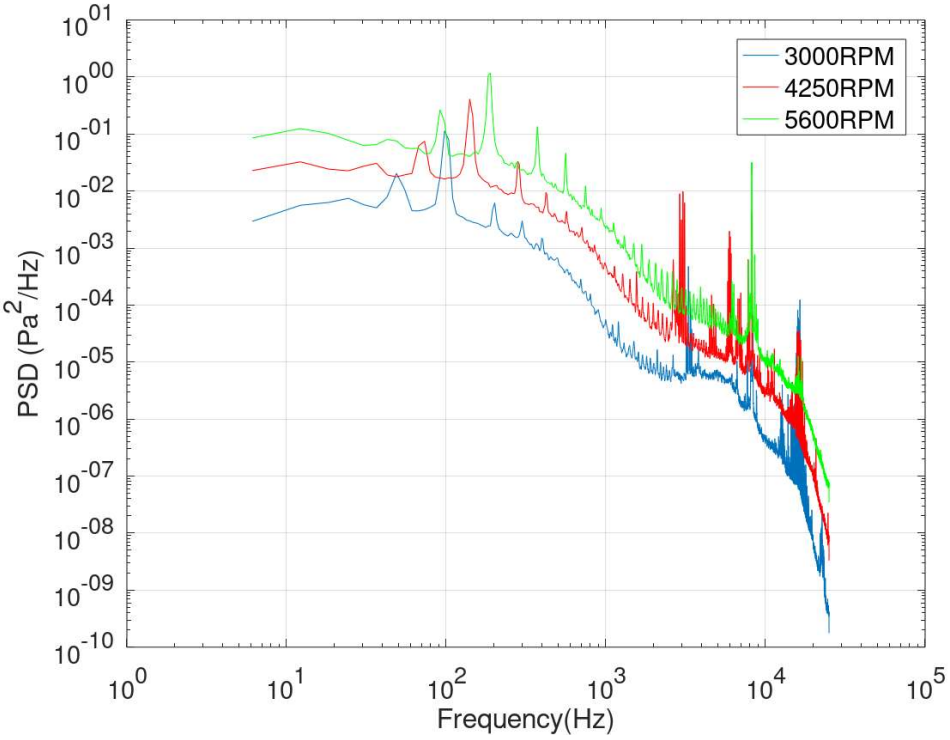

Figure 3.2. Speed comparison for a microphone placed underneath the motor housing.

Following this initial experiment, the microphone was then detached from the arm and mounted on a microphone stand underneath the assembly, approximately 0.5cm below the motor housing approximating the previous directly coupled mounting position. Mounting the microphone in this position allowed for the study of possible vibrational effects resulting from having the microphone rigidly mounted to the motor mount structure. The experimental setup is shown in Figure 3.3. A comparison of the measured response for the microphone mounted in each of these two locations is shown in Figure 3.4. It can be seen in the PSD that the B&K microphone measured a higher sound level when not attached to the motor housing. This is an unexpected result but may be due to the additional wind shielding resulting from the closer proximity to the housing for the rigidly attached microphone.

Figure 3.3. Experimental setup for non-rigidly attached microphone.

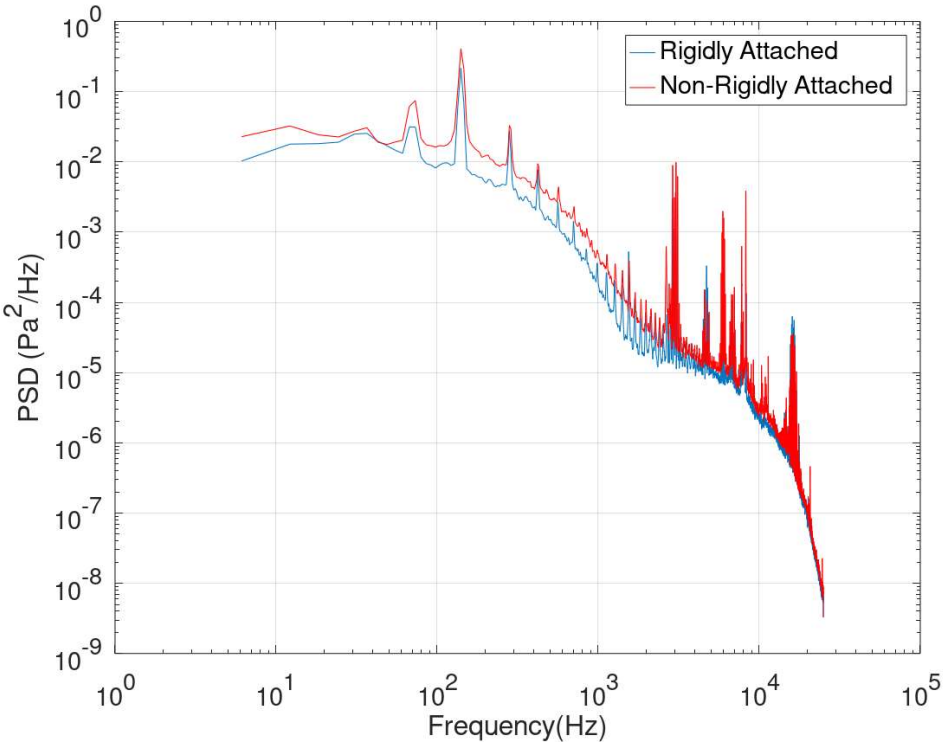

Figure 3.4. Comparison of microphone rigidly attached and non-rigidly attached.

Further experimentation allowed for identification of various noise sources. This was achieved by analyzing the PSD for constant microphone location while varying rotor speed, as well as varying microphone locations while keeping the rotor speed constant. The location of the microphone was adjusted by moving it along the shaft of the arm as measured from the end of the motor housing as well as adjusting the vertical distance between the shaft and the microphone. Examples of some of the setup locations are shown in Figures 3.5 and 3.6.

Figure 3.5. Microphone placed 11cm from the far end of the housing and 6cm below the arm.

Figure 3.6. Microphone placed 30cm from the far end of the housing and 18cm below the arm.

In general, the analysis of the PSD graphs can be broken up into two main groups, the lower frequency content (< 10^3 Hz) and the higher frequency content (> 10^3). These two groups are also separated into subgroups of the broadband acoustic noise and the narrowband harmonics within the broadband curves.

3.2 Anechoic Chamber Experiments

The experiments performed in the lab were recreated in the anechoic chamber for comparison. This was to investigate potential background noise interference from noise reflections in the lab. Identical motor speeds and microphone placements were used to be able to directly investigate the differences between the laboratory and the anechoic chamber. An example is shown in Figure 3.7. In this figure the microphone was placed 30.5cm from the end of the assembly along the arm and mounted 6 cm below the arm as compared to an equivalent lab setup shown in Figure 3.6.

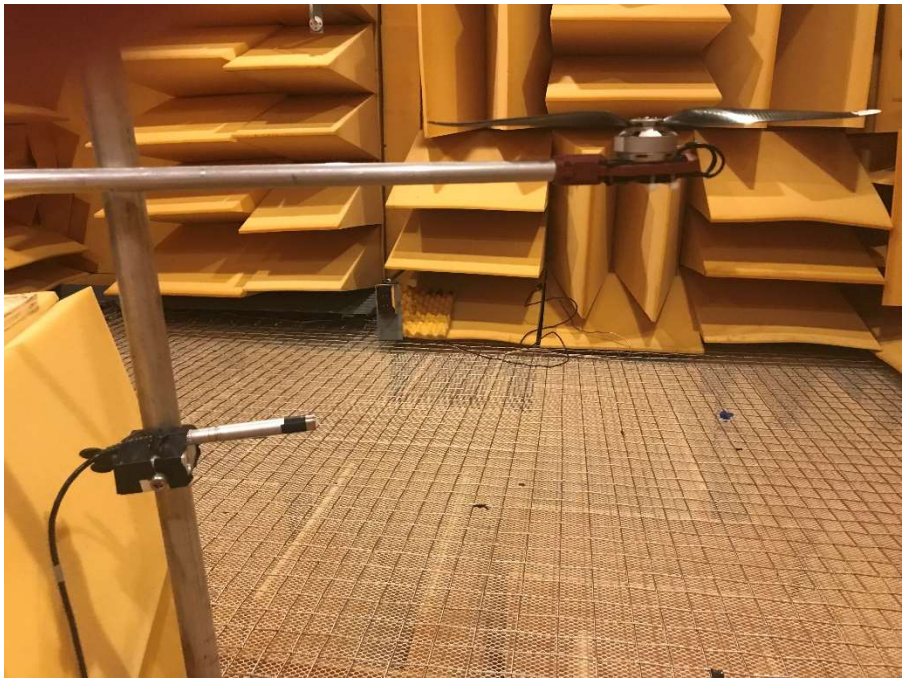

Figure 3.7. Experimental setup in the anechoic chamber

The overall amplitude and structure of the noise levels measured by the microphone in the anechoic chamber and the laboratory were comparable across the frequencies measured. The main difference between the two being that the lab experiment had a higher noise level in frequencies above 6 kHz. This comparison is shown in Figure 3.8.

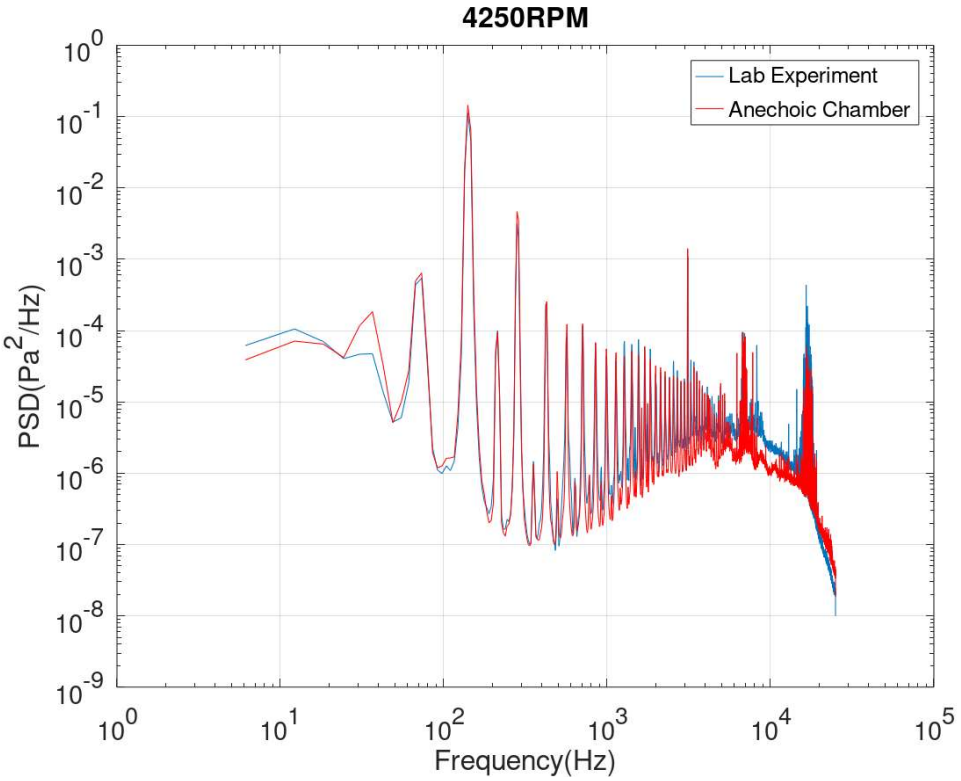

Figure 3.8. Noise comparison between lab and anechoic chamber for identical microphone position and rotor speed.

3.3 Low Frequency Range Analysis

The main hump in the lower frequencies centered around approximately 20Hz is predominately broadband noise, defined as noise whose energy is distributed over a wide section of the frequency range of interest and lacking minute structure. This noise source is

primarily turbulence noise from air flow generated by the spinning propeller that is directed downwards. One of the main dependencies of the turbulent noise is the speed at which the propeller is spinning. As the motor speed is increased, the general trend of the PSD curve is to shift towards the higher frequencies as shown in Figure 3.2. The maximum RPM does not follow this trend due to the max RPM of this setup being 5100 RPM. This speed is not significantly different enough to cause a further shift in the curve. A similar trend is shown in the data from the quadcopter assembly as shown in Figure 3.9.

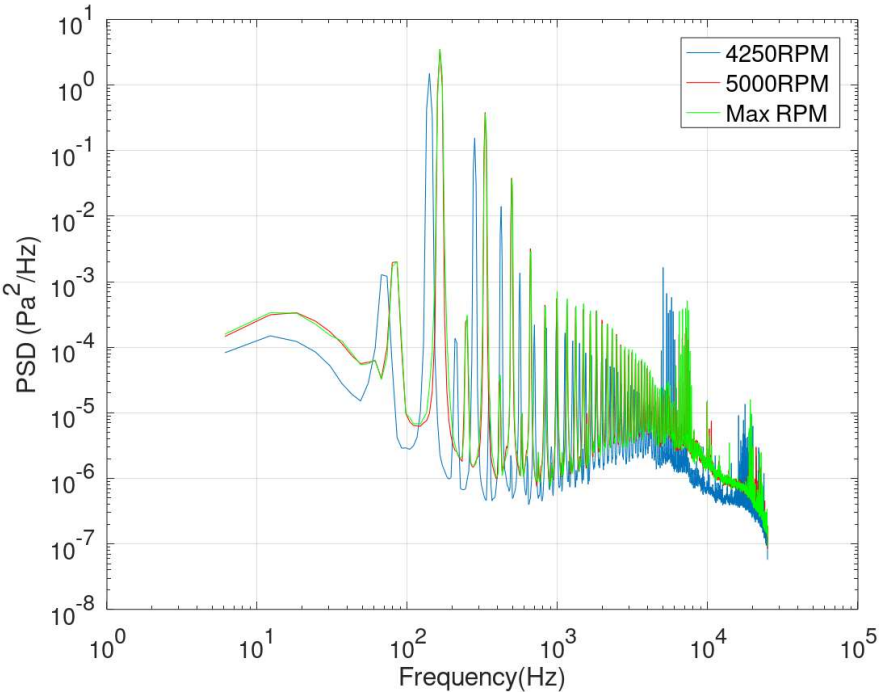

Figure 3.9. Speed comparison for single Tarot 690 quadcopter motor

The narrowband peaks are single point noise sources, followed by their harmonics. In this case single point refers to the sound being generated by a single characteristic. The sources of the initial peak are the noise and harmonics of the motor while it is spinning. The secondary peak, which has a greater magnitude, is due to the blade pass frequency of the propeller. This is

commonly referred to as “blade slap” and this noise source is generated when the rotating propeller passes over the arm and interferes with the flow produced by the rotor. The quadcopter single motor assembly shows similar results, with the main difference being the blade pass frequency is an order of magnitude larger. This significant difference in magnitude is due to the larger propellers of the quadcopter assembly. A comparison is shown in Figure 3.10.

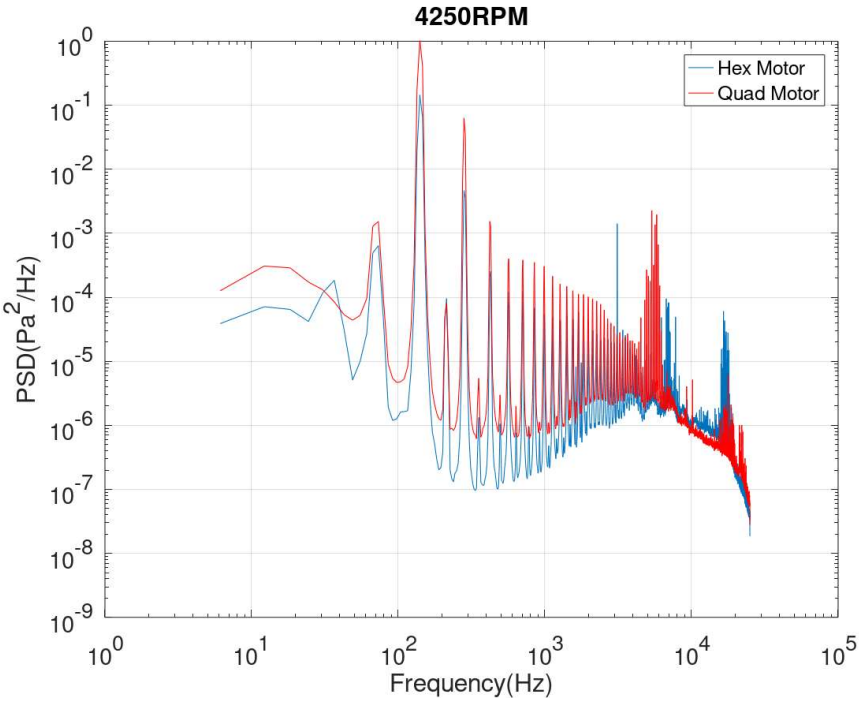

Figure 3.10. Comparison of hexacopter vs quadcopter assembly at identical speeds and microphone locations

3.4 High Frequency Range Analysis

In the high frequency range (above 5000Hz), there is another broadband noise curve along with groups of high frequency spikes. In the hexacopter motor-propeller assembly, the spikes appear at 2 kHz, 8 kHz, 10.5 kHz, and 11 kHz. Upon focusing in on these spikes they are

not single spikes, but tight groupings of spikes around certain frequencies. A close-up view of one of these groupings around 10.5kHz is shown in Figure 3.11.

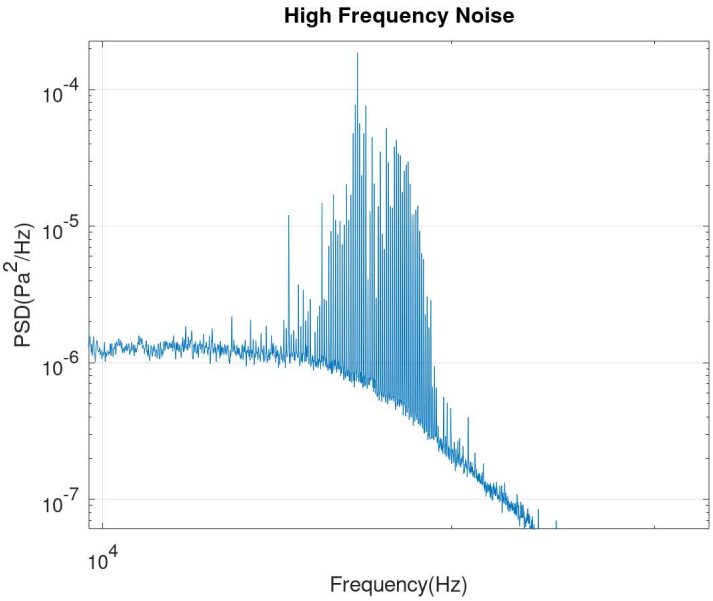

Figure 3.11. High frequency spikes

As the motor speed is increased these spikes grow in magnitude at first, and then quickly diminish after 4250 RPM. The spikes in the lower end of the frequency band (closer to 2 kHz) vary more than the spikes in the higher frequency. The higher frequency spikes do not display a frequency dependence on the speed of the motor, indicating that this is noise generated mechanically from within the motor. Audibly, the motors emit a high pitch noise that is most evident at 4250 PRM, and not heard at higher motor speeds. The propeller was removed to investigate if it was in fact motor generated noise. As shown in Figure 3.12 the only noise present with no propeller was the high frequency peaks indicating that they are caused by the motor.

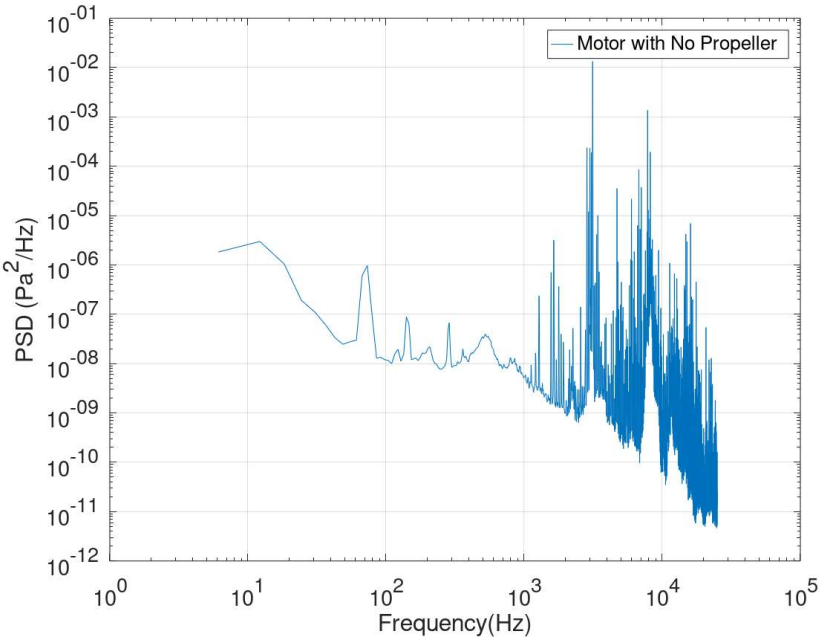

Figure 3.12. Motor spun at 4250RPM with no propeller attached

The origin of this noise is the electromagnetic coils in the center of the motor. The pulse-width modulation from the ESC will induce a magnetic charge on the stator coils and spin the motor causing an excitation and vibration due to electromagnetic forces. The excitation of the coils will cause electromagnetically induced acoustic noise, commonly referred to as coil whine. This noise is a natural resonance of the coils and is not dependent upon frequency.

The broadband noise portion of the measured curve needed further investigation to determine if it is acoustic or turbulent energy. A double microphone experiment was conducted in the anechoic chamber using two 1/2” B&K type 4190 microphones with 4” foam wind screen coverings. If acoustic, the time delay between the microphones would be consistent with the speed of sound, approximately 343m/s. The microphones were placed in the plane of the propeller and positioned radially outward from the center of the motor at distances of 100cm

and 114cm away. The motor speed was set at 4250 RPM, measured with an optical tachometer, with a Nexus conditioning amplifier set at a gain of 316mV/Pa for each microphone. An image of the setup is shown in Figure 3.13.

Figure 3.13. Double microphone setup in anechoic chamber.

A coherence plot of the data is shown in Figure 3.14 and implies the broadband noise curve in the high frequency range is generally coherent. Higher coherence at this short separation distance indicates that the noise is acoustic in nature. A calculation of the time delay of the signal received on the two microphones was performed with the results shown in Figure 3.15. A time delay of approximately 0.4mSec for the microphone spacing of 14cm as measured relative to the motor/propeller assembly produces a propagation speed of 350 m/s which is consistent with an expected speed of sound in the chamber in the range around 343 m/s. This indicates that the broadband noise curve is predominately composed of propagating acoustic

energy and not turbulent energy directly impending on the microphones. The source of this noise is still turbulence but it is turbulence generated acoustic energy, and for rotorcraft it is referred to as broadband acoustic energy.

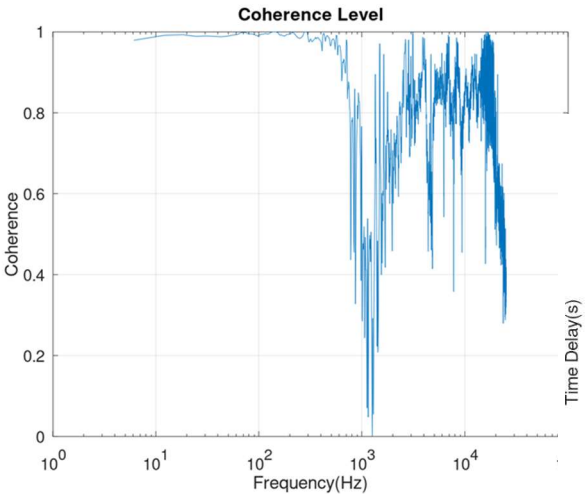

Figure 3.14. Coherence plot between microphones.

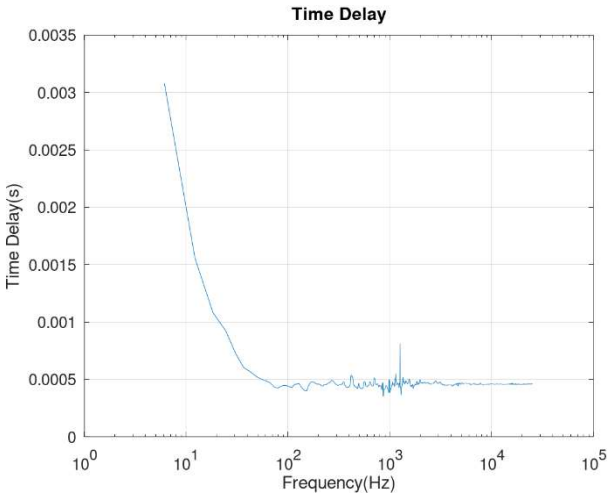

Figure 3.15. Time delay between microphones.

3.5 Multiple Motor Configuration

In the single motor configuration, the noise sources are distinguishable from each other and are identifiable. In practice a drone will have multiple motors in use with constantly varying speeds both individually and relatively to each other. To study these effects, a two-motor assembly was constructed as shown in Figure 3.16. The B&K microphone was placed centrally and 18cm below the edge of the frame. The motors were spun at similar speeds (within 100 RPM of each other, measured by the optical tachometer) and the PSD plot was produced. Figure 3.17 shows the PSD for a speed of 5000 RPM. The plot indicates that there is no new

phenomenon occurring when multiple motors are in use. The overall magnitude of the noise is increased with the structure of the curve similar to a single motor assembly.

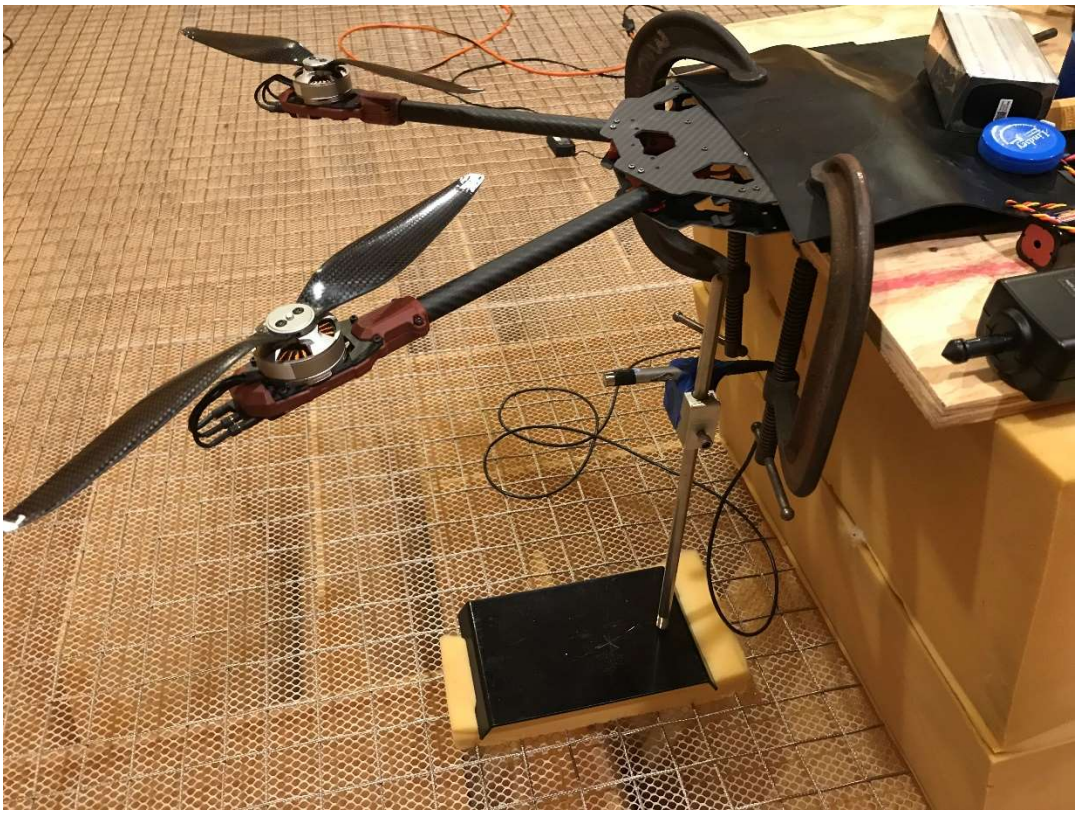

Figure 3.16. Multiple motor configuration for testing in anechoic chamber.

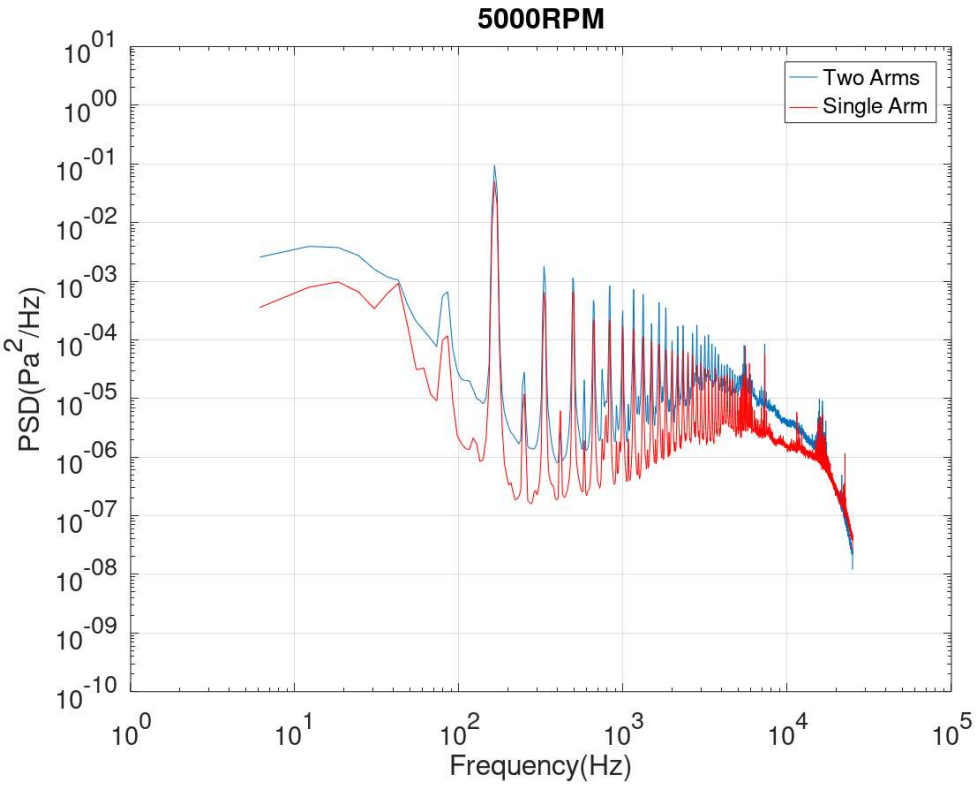

Figure 3.17. Multiple arm noise level comparison.

When the motor speeds differ by more than a few hundred RPM the characteristics of the different rotational rates begin to show up. For example, as discussed earlier the coil whine at 4250 RPM is much greater than at 5000 RPM. In order to determine how the motor speed vary in actual flight BL_Heli32 ESC's, which have the capability to directly measure motor rotational rate, were installed on the Tarot 680 Pro to obtain direct measurements of motors RPM during flight. The motor speed information was collected by the ground control station software Mission Planner and showed the RPM of each individual motor at a measurement rate of 200ms. Excluding advanced and drastic maneuvers, the motors were always within 100-200 RPM of each other and therefore the noise generated by the system should be similar to that of

the two-motor assembly but with a greater magnitude noise level due to presence of four additional motor/propeller assemblies and any additional turbulence resulting from flight.

Chapter 4

ADAPTIVE FILTER FOR TRANSIENT DETECTION

4.1 Least Mean Square Filter

The least mean square algorithm (LMS) is a form of adaptive filer invented first in 1960 by Bernard Widrow and Ted Hoff that uses a steepest descent method to find the desired results. Essentially, the filter seeks to find coefficients (weights) that minimize a least-squared error measure of performance, with the weights being updated as the algorithm is run. Due to the quadratic nature of the LMS there is a single extremum that is approached by the changing weights.

The LMS can be fully described using the set of equations:

$$\boldsymbol{W}(n) = [\omega_0(n)\ \omega_1(n) \ldots\ \omega_{L-1}(n)]^T$$

$$\boldsymbol{X}(n) = [x(n), x(n-1), \ldots, x(n-L+1)]^T$$

$$e(n) = d(n) - \boldsymbol{W}^T(n)\boldsymbol{X}(n)$$

$$W(n+1) = W(n) + \mu(n)e(n)\boldsymbol{X}(n)$$

Where ***W****(n)* is the coefficient vector, ***X****(n)* is the input signal vector, *d(n)* is the desired signal, *e(n)* is the error signal, and *μ(n)* is the step size [Widrow, B. and Hoff, 1960]. In this application the desired out put is the next measurement in the future.

The LMS filter is able to predict the desired results and return a given output. For the application of a HFDS, the algorithm will run until the predicted value of the next measurement is statistically significantly different from the actual value. This is treated as a transient detection and evaluated further.

An LMS filter is dependent on the input value scaling and requires a learning rate that provides a stable filter. Achieving an optimum learning rate for the algorithm is possible for analysis of sets of data, however it is not robust enough for similar learning rates to be used on multiple sets of data. The learning rate needs to be evaluated and chosen specifically for each situation, which requires significant testing and analysis.

4.2 Normalized Least Mean Square Filter

For a chosen step size that is small to guarantee stability of the algorithm, the convergence speed is unnecessarily slow for a small signal power. This can be improved with a normalized step size of

$$\mu(n) = \frac{\bar{\mu}}{\delta + L\widehat{\sigma_x^2}(n)}$$

Where $\widehat{\sigma_x^2}(n)$ is an estimate of the input signal power, $\bar{\mu}$ is a constant, and δ is a small constant to avoid a divide-by-zero. For an estimate of the input signal power, a lowpass filter can be applied to the sequence $x^2(n)$. The two commonly used estimates include

Exponentially weighted estimate:

$$\widehat{\sigma_x^2}(n) = (1-c)\widehat{\sigma_x^2}(n-1) + cx^2(n)$$

Sliding-window estimate:

$$\widehat{\sigma_x^2}(n) = \frac{1}{N}\sum_{i=0}^{N-1} x^2(n-i)$$

Where the parameters *c*, 0 < *c* << 1 and *N*, *N* ≥ *L* control the effective memories of the two estimators.

If a sliding window estimate of length *N* = *L* is chosen, the LMS filter with normalized step size becomes

$$\boldsymbol{W}(n+1) = \boldsymbol{W}(n) + \frac{\bar{\mu}e(n)}{p(n)}\boldsymbol{X}(n)$$

$$p(n) = \delta + \|\boldsymbol{X}(n)\|^2$$

Where $\|\boldsymbol{X}(n)\|^2$ is the L_2-norm of the input signal vector. The value of *p(n)* can be updated recursively as

$$p(n) = p(n-1) + x^2(n) - x^2(n-L)$$

This adaptive filter is known as the Normalized Least Mean Square (NLMS) adaptive filter, and it has two properties that a very useful:

- The NLMS is guaranteed to converge for any value of $\bar{\mu}$ in the range $0 < \bar{\mu} < 2$ regardless of the statistics of the input signal.
- With the proper $\bar{\mu}$ choice, the filter can often converge faster that the LMS filter.

These properties allow for an easier selection of the step size μ and a more uniform convergence than the LMS filter. [Farden, 1981]

4.3 NLMS filter for Transient Detection

A NLMS algorithm was written in the programming language Python using Enthought Canopy for evaluation of data taken during field testing of the Tarot 680 Pro hexacopter multi-rotor drone. The field test was conducted at Water Valley Airport in Water Valley Mississippi and consisted of flying the multi-rotor drone with an onboard microphone array while a propane cannon was fired. The microphone array was a Zylia ZM-1, 19 channel spherical array and it was mounted on the Tarot hexacopter, as shown in Figure 4.1. This array uses digital microelectro-mechanical systems (MEMS) microphones that give a digital output of the measured acoustic signal. The propane cannon was fired at various times as the multi-rotor drone was flown directly away from the propane cannon location.

Figure 4.1. Tarot 680 Pro with Zylia ZM – 1 spherical array

For initial data analysis a single microphone channel was evaluated on a ten second file sampled at 50,000 sps. The microphone channel was chosen arbitrarily and used as a basis to study the effects of varying $\bar{\mu}$, filter order values, and the false alarm rate (α). The false alarm rate value is set assuming that the data is a normal distribution and α is the upper and lower limit cutoff. The α value was initially set as $1 - {}^{1}/_{5e10}$ The standard deviation of the error was the value studied for each case, allowing for analysis of filter and step sizes. To study these effects the error and standard deviation of the error was evaluated for the NLMS algorithm on data that was both non-decimated as well as decimated by factors of 2, 5, and 10 on a dataset that was known to have a propane cannon shot of magnitude significantly larger than the background noise level.

4.4 NLMS Filter Results

The non-decimated data produced the standard deviation of the error shown in Table 4.1. The data shows that the filter works well for varying step sizes ($\bar{\mu}$) and filter order (p) due to the low standard deviation of the error. The results show that a decreasing step size and an increasing filter order have a trend of decreasing the standard deviation of the error. Once the step size is further decreased however it causes an increase in the standard deviation of the errors and is not as effective. Further study was performed with smaller filter orders and step sizes, to match a realistic step size value and is shown that too small of a filter order causes a negative effect on the standard deviation. The results from this study are shown in Table 4.2.

		p				
		10	**20**	**50**	**100**	**500**
μ	**1**	0.0645	0.0644	0.0625	0.0521	0.042
	0.75	0.0576	0.0574	0.0555	0.0469	0.0412
	0.5	0.0526	0.0522	0.0504	0.0444	0.0407
	0.1	0.0457	0.0449	0.0445	0.0445	0.0437
	0.01	0.0445	0.0447	0.0479	0.0539	0.0554

Table 4.1. Standard deviation of the error for NLMS algorithm

		p				
		10	**20**	**30**	**40**	**50**
	0.1	0.0457	0.0449	0.0449	0.0446	0.0445
	0.01	0.0446	0.0448	0.0457	0.0466	0.0479
μ	**0.001**	0.0483	0.0519	0.0557	0.59	0.0626
	0.0001	0.0623	0.0705	0.0783	0.0821	0.0886
	0.00001	0.0874	0.1025	0.1172	0.1257	0.1327

Table 4.2. Standard deviation of errors for smaller step sizes

The decimated data allows for comparable standard deviations, with a smaller step size. A smaller step size is computationally less taxing and allows for faster algorithm run times. A decimation by a factor of 2 shows that using a step size of 0.1 and a filter order of 10 obtains a standard deviation that is comparable to the non-decimated data with a step size of 0.1 and filter order of 50. A comparison of the standard deviations of the errors for the decimated data is given in Tables 4.3 and 4.4.

		p				
		2	**4**	**6**	**8**	**10**
μ	**0.1**	0.0831	0.0664	0.0603	0.0554	0.0524
	0.01	0.0709	0.0633	0.0587	0.0556	0.0561
	0.001	0.0672	0.0644	0.0635	0.0649	0.0662
	0.0001	0.0694	0.0748	0.0786	0.0817	0.0846
	0.00001	0.0795	0.093	0.1007	0.1053	0.1122

Table 4.3. Standard deviation of errors with a decimation by a factor of 2

		p				
		2	**4**	**6**	**8**	**10**
μ	**0.1**	0.1283	0.0868	0.0796	0.0748	0.0681
	0.01	0.1077	0.0829	0.0783	0.0775	0.0778
	0.001	0.1043	0.0861	0.0917	0.09	0.0932
	0.0001	0.1062	0.1069	0.1143	0.1146	0.1189
	0.00001	0.1136	0.1254	0.1458	0.1661	0.1846

Table 4.4. Standard deviation of errors with a decimation by a factor of 5

The low standard deviations give a level of confidence to predictions of when an alarm has been triggered. The algorithm is adjusted slightly to trigger an "alarm" when the algorithm fails to predict the future value by a statistically significant margin. In preforming this study α is the value that reduces or increases the false alarm rate. As the value of α is increased to values closer to 1, the false alarm rate decreases by a significant margin. Table 4.5 shows the false alarm rate for varying filter order and step sizes. The alarms triggered are for every instance the algorithm failed to predict the next value. These triggers are only for a single microphone channel and when multiple channels are utilized in the algorithm a comparison is used and only triggers at the same or similar locations are kept. Table 4.6 indicates that there is significant background noise reduction when utilizing a NLMS adaptive filter.

		p		
		50	**100**	**150**
	0.5	0.025% (F)	0.012% (F)	0.012% (F)
μ	**0.1**	0.029% (D)	0.029% (D)	0.021% (D)
	0.01	0.027% (D)	0.019%(D)	0.017% (D)

Table 4.5. False alarm rate for $\alpha = 1 - 1/5e15$, D = successful detection, F = only false alarms

		p		
		50	**100**	**150**
	0.5	47.60%	47.60%	48.60%
μ	**0.1**	43.29%	43.29%	43.80%
	0.01	43.29%	45.70%	47.60%

Table 4.6. Noise level reduction.

This algorithm has not yet been implemented on continuously running data from microphones on a multi-rotor drone, but shows an example of an adaptive filter that works in accurately identifying if there is a shot present in acoustic data.

CHAPTER 5

CONCLUSIONS

Noise source identification of a multi-rotor drone was achieved by analyzing the noise characteristics present in a PSD graph. The experimental results show that all primary noise sources were identified and have been characterized by their frequencies. The results also show that this characterization is consistent with multiple motors in simultaneous operation with no significant changes in the overall sound signature resulting from their operation.

It is also shown that an adaptive filter algorithm is able to successfully identify a transient signal from a microphone source mounted on a multi-rotor drone. The NLMS algorithm when run on recorded data accurately triggers if a propane cannon shot is in the data. The results of this testing show that an integrated system running a similar algorithm will be able to successfully trigger an alarm for the user operating the HFDS. The successful trigger will then allow for a direction of arrival estimation to be made.

The acoustic characterization of a multi-rotor drone that is presented provides a compliment to research in implementing a HFDS on a multi-rotor drone. The characterization of the noise produced by a multi-rotor drone could be an inspiration for further studies on mitigating the noise of a multi-rotor drone as well as understanding the noise produced by brushless electric motors.

BIBLIOGRAPHY

Brackley, M., & Pollock, C. (2000). Analysis and reduction of acoustic noise from a brushless DC drive. *IEEE Transactions on Industry Applications*, *36*(3), 772–777. https://doi.org/10.1109/28.845052

Brentner, K. S., & Farassat, F. (2003). Modeling aerodynamically generated sound of helicopter rotors. *Progress in Aerospace Sciences*, *39*(2), 83–120. https://doi.org/https://doi.org/10.1016/S0376-0421(02)00068-4

Carley, M. (2012). *Turbulence and noise*.

Cho, Y. T. (2018). Characterizing sources of small DC motor noise and vibration. *Micromachines*, *9*(2). https://doi.org/10.3390/mi9020084

Corcos, G. M. (1963). Resolution of Pressure in Turbulence*. In *THE JOURNAL OF THE ACOUSTICAL SOCIETY OF AMERICA* (Vol. 35, Issue 2). http://asadl.org/journals/doc/ASALIB-home/info/terms.jsp

de Jong, B. A. (2016). *Development of scaling methods for broadband turbulent noise in internal flow devices by means of experiments and CFD*.

Fernandes, R. P., Apolinário, J. A., & Ramos, A. L. L. (2017, June 13). Bearings-only aerial shooter localization using a microphone array mounted on a drone. *LASCAS 2017 - 8th IEEE Latin American Symposium on Circuits and Systems, R9 IEEE CASS Flagship Conference: Proceedings*. https://doi.org/10.1109/LASCAS.2017.7948081

George, A. R., & Chou, S.-T. (1984). *Broadband Rotor Noise Analyses*.

Goering, A. (2018). *UAV NOISE REDUCTION*.

Kloet, N., Watkins, S., & Clothier, R. (2017a). Acoustic signature measurement of small multi-rotor unmanned aircraft systems. *International Journal of Micro Air Vehicles*, *9*(1), 3–14. https://doi.org/10.1177/1756829316681868

Kloet, N., Watkins, S., & Clothier, R. (2017b). Acoustic signature measurement of small multi-rotor unmanned aircraft systems. *International Journal of Micro Air Vehicles*, *9*(1), 3–14. https://doi.org/10.1177/1756829316681868

Koops, H.V., Garg, K., Kim, M., Li, J.Z., Volk, A., & Franchetti, F. (2017). Prediction of Quadcopter State through Multi-Microphone Side-Channel Fusion.

Lee, H. J., Chung, S. U., & Hwang, S. M. (2008). Noise source identification of a BLDC motor. *Journal of Mechanical Science and Technology*, *22*(4), 708–713. https://doi.org/10.1007/s12206-008-0110-9

Leverton, J. W. (2014). Helicopter Noise: What is the Problem? *VERTIFLITE*, *60*(2). www.vtol.org/noise

Lighthill, M. J. (1952). On sound generated aerodynamically I. General theory. *Royal Society Publishing*, *211*(1107). http://rspa.royalsocietypublishing.org/Downloadedfrom

Lighthill, M. J. (1954). On sound generated aerodynamically II. Turbulence as a source of sound. *Royal Society Publishing*, *222*(1148).

Made, J. E., & Kurtz, D. W. (1970). *N A Review of Aerodynamic Noise From Propellers, Rofors, and Liff Fans*. https://ntrs.nasa.gov/search.jsp?R=19700005920

Mandic, D. P. (2004). A generalized normalized gradient descent algorithm. In *IEEE Signal Processing Letters* (Vol. 11, Issue 2 PART I, pp. 115–118). https://doi.org/10.1109/LSP.2003.821649

Molino, J. A. (1982). *Should Helicopter Noise Be Measured Differently From Other Aircraft Noise?-A Review of the Psychoacoustic Literature*.

Nakadai, K., Kumon, M., Okuno, H. G., Hoshiba, K., Wakabayashi, M., Washizaki, K., Ishiki, T., Gabriel, D., Bando, Y., Morito, T., Kojima, R., & Sugiyama, O. (2017). Development of microphone-array-embedded UAV for search and rescue task. *2017 IEEE/RSJ International Conference on Intelligent Robots and Systems (IROS)*, 5985–5990. https://doi.org/10.1109/IROS.2017.8206494

Paterson, R. W., & Amiet, R. K. (1979). *Noise of a Model Helicopter Rotor Due to Ingestion of Turbulence*. https://ntrs.nasa.gov/search.jsp?R=19800002821

Tinney, C. E., & Sirohi, J. (2018). Multirotor Drone Noise at Static Thrust. *AIAA Journal*, *56*(7), 2816–2826. https://doi.org/10.2514/1.J056827

Wang, L, & Cavallaro, A. (2016). Ear in the sky: Ego-noise reduction for auditory micro aerial vehicles. *2016 13th IEEE International Conference on Advanced Video and Signal Based Surveillance (AVSS)*, 152–158. https://doi.org/10.1109/AVSS.2016.7738063

Wang, Lin, & Cavallaro, A. (2018). Acoustic sensing from a multi-rotor drone. *IEEE Sensors Journal*, *18*(11), 4570–4582. https://doi.org/10.1109/JSEN.2018.2825879

Yen, B., Hioka, Y., & Mace, B. (2018). Improving Power Spectral Density Estimation of Unmanned Aerial Vehicle Rotor Noise by Learning from Non-Acoustic Information. *2018 16th International Workshop on Acoustic Signal Enhancement (IWAENC)*, 545–549. https://doi.org/10.1109/IWAENC.2018.8521324

VITA

EDUCATION

Masters of Science in Physics, University of Mississippi
Expected Graduation, May 2020
Thesis: Acoustic Modeling of a UAS for use in a Hostile Fire Detection System

Bachelor of Science, Mississippi College
Major: Physics
Minor: Mathematics

RESEARCH EXPERIENCE

Research Assistant, The University of Mississippi — March 2019 - Present

Advisors: Wayne Prather, Garth Frazier

- Modeled acoustic noise of a multi-rotor drone for use in a hostile fire detection system
- Developed and implemented signal processing and data analysis techniques for hostile fire detection system
- Repaired and maintained multi-rotor drones

Teaching Assistant, The University of Mississippi — July 2018 – December 2018

Advisor: Marco Cavaglia

- Designed machine learning algorithms for data collected from LIGO scientific collaboration

SELECTED ACTIVITIES

Teaching Assistant, The University of Mississippi — August 2017 – December 2019

- Taught Astronomy 103 and Astronomy 104 labs
    - Topics included solar system and star formation, deep sky objects, and mathematical representations of the universe

- Taught Honors College students astrophotography and deep sky imaging

- Taught image processing techniques for astrophotography
    - Used software such as CCDops and Photoshop to enhance pictures

Physics Tutor, Mississippi College September 2016 – May 2017

- Tutored Physics students as needed throughout the semester
    - Taught general algebra and calculus-based physics

ORAL PRESENTATION

W. Frazier, W. Prather, K. Kurpakus. Development of Acoustic Arrays on Multi-Rotor Unmanned Aerial Systems. Presented at: 2019 Meeting of the Military Sensing Symposia (MSS) Specialty Groups on: Battlespace Acoustic, Seismic, Magnetic, and Electric-Field Sensing and Signatures, National Symposium on Sensor and Data Fusion; 2019 Oct 21-24; San Diego, CA